Nanoscale metal-organic frameworks for the delivery of nucleic acids to cancer cells

Xue Li [a,1], Morgan Chandler [b,1], Yelixza I. Avila [b], Sandra I. Arroyo-Becker [b], Gilles Patriarche [c], Antonio Vargas-Berenguel [d], Juan M. Casas-Solvas [d], Kirill A. Afonin [b,*], Ruxandra Gref [a,*]

[a] Université Paris-Saclay, CNRS, Institut des Sciences Moléculaires d'Orsay, 91405 Orsay, France
[b] Nanoscale Science Program, Department of Chemistry, University of North Carolina at Charlotte, Charlotte, NC 28223, USA
[c] Université Paris-Saclay, CNRS, Centre de Nanosciences et de Nanotechnologies (C2N), 91120 Palaiseau, France
[d] Department of Chemistry and Physics, University of Almería, Ctra de Sacramento s/n, 04120 Almería, Spain

ABSTRACT

Therapeutic nucleic acids (TNAs) are gaining increasing interest in the treatment of severe diseases including viral infections, inherited disorders, and cancers. However, the efficacy of intracellularly functioning TNAs is also reliant upon their delivery into the cellular environment, as unmodified nucleic acids are unable to cross the cell membrane mainly due to charge repulsion. Here we show that TNAs can be effectively delivered into the cellular environment using engineered nanoscale metal-organic frameworks (nanoMOFs), with the additional ability to tailor which cells receive the therapeutic cargo determined by the functional moieties grafted onto the nanoMOF's surface. This study paves the way to integrate the highly ordered programmable nucleic acids into larger-scale functionalized nanoassemblies.

1. Introduction

Therapeutic nucleic acids (TNAs) offer highly modular approaches to the treatment of various diseases. TNA technology has allowed rapid breakthroughs such as the mRNA vaccines against SARS-CoV-2 (Jackson et al., 2020; Panigaj et al., 2021). TNAs' clinical development is expanding as shown by the increasing repertoire that has been approved by the United States Food and Drug Administration (FDA) and European Medicines Agency (EMA) (Johnson et al., 2021; Kulkarni et al., 2021). However, the efficacy of intracellularly functioning TNAs is reliant upon their delivery into the cellular environment, as unmodified nucleic acids are unable to cross the cell membrane due to their negative charge. As a result, one of the major challenges of TNA research is the need for engineering biocompatible and versatile nanocarriers. Nanocarriers offer novel opportunities to achieve optimal multimodal delivery, targeted site specificity, and immunorecognition. Each of these characteristics can be tuned depending on the application and the carrier. Lipid-based (Kim et al., 2020), polymeric (Halman et al., 2020), mesoporous silica nanoparticles (Juneja et al., 2020; Rackley et al., 2018), poly-silsesquioxane (Juneja et al., 2019), and cell-derived carriers such as

exosomes (Ke and Afonin, 2021; Nordmeier et al., 2020) are examples of nanocarriers that were shown to effectively deliver nucleic acid cargos into the cellular environment. Interstingly, the immunostimulatory effect of TNAs was reduced when delivered with a nanocarrier as compared to their delivery with commercially available lipids (Avila et al., 2021; Halman et al., 2020). Therefore, there is a great interest in expanding the possibilities of TNA delivery by adding new functionalities to their nanocarries. It was our aim here to engineer multifunctional TNA nanocarriers in a sustainable, versatile manner, and which could also provide imaging ability, targeting of tumor cells, and delivery of anticancer drugs.

Hybrid nanoscale metal-organic frameworks (nanoMOFs) with large pore volumes and surface areas are a new class of versatile porous materials formed by the coordination of metal clusters and organic ligands (Férey et al., 2005). More particularly, the biodegradable iron trimesate MIL-100(Fe) nanoMOFs (MIL stands for Materials of Institute Lavoisier) are considered among the most efficient materials as drug carriers (Ettlinger et al., 2022) because of the following unique properties: 1) high drug loading capacity for drugs with different physicochemical properties (Horcajada et al., 2009); 2) easily engineered multifunctional

surfaces composed of targeting moieties (Agostoni et al., 2015; Qiu et al., 2021; Mokhtarian et al., 2022); and 3) possibilities to conveniently attach fluorescent moieties for imaging purposes (Li et al., 2020a; Qiu et al., 2020b).

Among the various nanoMOFs used for biomedical applications, the MIL-100(Fe) nanoMOFs are among the best-documented in terms of biocompatibility (Ding et al., 2022). MIL-100(Fe) nanoMOFs were shown to be non-toxic both *in vitro* and *in vivo* (Baati et al., 2013; Simon-Yarza et al., 2016; He et al., 2021; Simon-Yarza et al., 2017). They are built from iron trimers which assemble with organic trimesate linkers to form an open porous structure with cages of 5 and 9 Å in which active molecules with various physicochemical properties can be incorporated (He et al., 2021; Wang et al., 2018; Sun et al., 2020; Li et al., 2020b).

For instance, MIL-100(Fe) nanoMOFs were reported to act as "nanosponges," soaking up gemcitabine monophosphate (Gem-MP), from its aqueous solution with high drug payload (up to 25 wt%) (Rodriguez-Ruiz et al., 2015). The drug was incorporated with yields >98%, due to the strong coordination of the phosphate group in Gem-MP with the accessible unsaturated metal sites of the Fe trimers. Advantageously, this almost perfect encapsulation avoided the need of nanoMOF purification from non-encapsulated drug. Furthermore, in order to improve the colloidal stability, enable stealth property and obtain targeting effects, the nanoMOF external surface was modified based on the same principle: spontaneous coordination between available Fe sites at the surface and phosphate moieties in the coating material. To prevent the penetration of the coating materials into the nanoMOFs' pores, bulky molecules with dimensions larger than the pore size, such as cyclodextrin (CD) derivatives (Agostoni et al., 2015; Cutrone et al., 2019a; Qiu et al., 2021), dextran with poly(ethylene glycol) (PEG) side chains (Cutrone et al., 2019b), and fluorescent CD copolymers (Qiu et al., 2020b) were spontaneously and firmly adsorbed. In other approaches, the nanoMOFs' external surface was modified with heparin, hyaluronic acid, CD-based polymers, lipids and crosslinked PEG chains (Bellido et al., 2015; Cutrone et al., 2019b; Gimenez-Marques et al., 2018; Li et al., 2020b; Qiu et al., 2020a; Sun et al., 2021). In addition, the MIL-100(Fe) nanoMOFs were synthesized by a hydrothermal method, where no organic solvents nor surfactants were employed. In a nutshell, all the steps involved in the preparation of drug-loaded and surface functionalized nanoMOFs were "green," making them attractive for drug delivery, and especially for the hydrolysable TNAs which need to be protected from nuclease degradation when exposed to biological media. However, there are still scarce examples of nanoMOFs engineered as carriers for TNAs (Peng et al., 2018; Teplensky et al., 2019) with several works reporting the MOF-assisted delivery of pooled siRNAs (He et al., 2014), single-stranded DNAs (Peng et al., 2018), as well as miRNAs and DNAzymes (Ni et al., 2022).

Here, we demonstrate the association of TNA cargos with MIL-100 (Fe) nanoMOFs for efficient delivery to cancer cell lines HeLa and MDA-MB-231. We start by characterizing the binding of DNA duplexes to nanoMOFs as a foundation, and later introduce Dicer Substrate (DS) RNAs to the system, which are designed to carry out gene silencing *via* RNA interference. We also investigated the uptake efficacy of fluorescently labeled double stranded DNAs delivered into human cervical and breast cancer cell lines using nanoMOFs. Gene silencing efficiency was studied in MDA-MB-231 breast cancer cells, using DS RNAs associated to nanoMOFs. Finally, we demonstrated the multimodality of nanoMOFs by introducing multiple functionalities including association of Gem-MP, fluorescent moieties and ligands to target cancer cells. It is worth mentioning that CD bearing both phosphate and mannose moieties (P-CD-M) were employed to functionalize nanoMOFs and their mannose moieties enabled the targeting of cancer cells (Agostoni et al., 2015). This concept was used here to target TNAs and Gem-MP cargos within MIL-100(Fe) nanoMOFs to MDA-MB-231 cells hyper-expressing mannose receptors (Li et al., 2020a, 2020b, 2020c). The present study serves as a proof of concept for associating large nucleic acid assemblies and TNAs to nanoMOFs, as well as combining multiple strategies and functionalities within this tunable and versatile system.

2. Experimental

2.1. Materials and reagents

2.1.1. Chemical materials

Iron (III) chloride hexahydrate (FeCl$_3$·6H$_2$O, Alfa Aesar, Schiltigheim, France, 98%), 1,3,5-benzenetricarboxylic acid (BTC, Sigma-Aldrich, Saint-Quentin-Fallavier, France, 95%) and absolute ethanol (EtOH, Carlo Erba, Val-de-Reuil, France, 99%) were used for the synthesis of MIL-100(Fe). 2′,2′-Difluorodeoxycytidine monophosphate (Gem-MP) was purchased from Toronto Research Chemicals (Canada). Triethylamine acetate and methanol (HPLC grade) were purchased from Sigma-Aldrich (France) as mobile phase for detection of Gem-MP. Water was purified by a Millipore MilliQ system.

Dry *N,N*-dimethylformamide (DMF) (AcroSeal, 99.8%) was purchased from Acros. Sodium hydroxide (NaOH, ≥99.0%), potassium chloride (KCl, Sigma-Aldrich, ≥99%), hydrochloric acid (HCl, 37%) were purchased from Merck Sigma-Aldrich (Saint-Quentin-Fallavier, France) for the synthesis of CD bearing both phosphate and mannose moieties (P-CD-M).

For the synthesis of adamantane-rhodamine (Ad-Rh), DMF and dichloromethane (CH$_2$Cl$_2$) were distilled from calcium hydride, under nitrogen atmosphere. All reactions involving air- or water-sensitive compounds were routinely conducted in glassware which was flame-dried under a positive pressure of nitrogen or argon. 1-Ethyl-3-(3-dimethylaminopropyl)-carbodiimide (EDCI), hydroxybenzotriazole (HOBt), ethyl ether (Et$_2$O), and 2,2′-(ethylendioxy)bis(ethylamine) were obtained from Merck Sigma-Aldrich (Saint-Quentin-Fallavier, France).

2.2. General methods

2.2.1. NanoMOFs preparation

MIL-100(Fe) iron trimesate nanoMOFs were synthesized by adapting a previously described method (Agostoni et al., 2013; Li et al., 2020c). Briefly, nanoMOFs were obtained by microwave-assisted hydrothermal synthesis from a mixture of iron chloride (8.97 mmol) and BTC (4.02 mmol) in 30 mL of deionized water. The mixture was heated for 6 min at 130 °C under stirring in a microwave oven (Mars-5, CEM, US), with an applied power of 1600 W. The resulting nanoMOFs were recovered by centrifugation for 10 min at 10,000 *g* and purified by six washing steps using absolute ethanol. A last centrifugation at 5000 *g* was performed during 10 min in absolute ethanol to recover the smallest particles in the supernatants as a suspension of monodisperse nanoparticles. NanoMOFs were stored in ethanol until use. To prepare nanoMOFs for complexation, the samples were first centrifuged at 10,000 *g* for 10 min. The supernatant was removed and the pellet was dispersed in water (HyClone, Molecular Biology Grade). This was repeated twice and the final volume of water for resuspension was chosen to bring the final concentration to 1 mg/mL of nanoMOFs.

The nanoMOFs' BET specific surface was measured by nitrogen sorption experiments at 77 K using an ASAP 2020 (Micromeritics) after sample's outgassing at 100 °C overnight under secondary vacuum.

2.2.2. P-CD-M synthesis

Heptakis{6-desoxi-6-{4′-[14″-*O*-(α-ᴅ-mannopyranosyl)-2″,5″,8″,11″,14″-pentaoxatetradecyl]-1*H*-1,2,3-triazol-1′-yl}}ciclomaltoheptose phosphate sodium salt (P-CD-M) was synthesized as previously described (Cutrone et al., 2019a). Briefly, P$_2$O$_5$ (510 mg, 3.6 mmol) was suspended in dry DMF (13 mL) and sonicated for 30 min, then heptakis(6-deoxy-6-{4′-[14″-*O*-(2‴,3‴,4‴,6‴-tetra-O-acetyl-α-ᴅ-mannopyranosyl)-2″,5″,8″,11″,14″-pentaoxatetradecyl]-1*H*-1,2,3-triazol-1′-yl)ciclomaltoheptose (356 mg, 0.068 mmol) was added. The mixture was stirred at 40 °C until no starting material was observed (after 5 h) by TLC and then stirred for 12 h at room temperature at pH

11–13 (which was maintained by addition of 1 M aqueous NaOH as needed). The solution was then neutralized with 5% aqueous HCl and the solvent evaporated under high vacuum. The residue was dissolved in the minimum amount of H_2O, syringe filtered (nylon 0.45 μm), and dialyzed (2000 MWCO) against distilled water by changing dialysate solution every 3 h until its conductivity was stable and below 1 μS/cm (5 days for final value of 0.98 μS/cm) to yield P-CD-M (806 mg) as a white solid after lyophilization. NMR data agreed with those previously reported (Cutrone et al., 2019a).

2.2.3. Ad-Rh synthesis

Prior to the synthesis of Ad-Rh, the compound 3-{[2-(2-{2-[2-(adamantan-1-yl)acetamido]ethoxy}ethoxy)ethyl]carbamoyl}propanoic acid (Li et al., 2020a) and rhodamine piperazine (Nguyen and Francis, 2003) were synthesized as described previously. Briefly, to a mixture of rhodamine piperazine (120 mg, 0.22 mmol) and 3-{[2-(2-{2-[2-(adamantan-1-yl)acetamido]ethoxy}ethoxy)ethyl]carbamoyl}propanoic acid (113 mg, 0.26 mmol) in DMF (3 mL) were added HOBt (10 mg, 0.07 mmol), EDCI (56 mg, 0.29 mmol) and Hünig's base (148 mg, 1.15 mmol). After 24 h reaction at room temperature, the resulting Ad-Rh was extracted and purified.

2.2.4. Nucleic acid preparation

DNA duplexes were assembled with Alexa Fluor 488-labeled oligos. Dicer Substrate (DS) RNA duplexes were prepared against GFP and survivin. All sequences are available in the Supporting Information and were purchased from Integrated DNA Technologies, Inc. To assemble each duplex, the corresponding sequences were added in an equimolar ratio in water (HyClone, Molecular Biology Grade) and heated to 95 °C for 2 min. Following this, assembly buffer was added to a final concentration of 89 mM tris-borate (pH 8.2), 2 mM $MgCl_2$, 50 mM KCl. The duplex was then incubated at room temperature for 20 min and stored on ice or at 4 °C for all subsequent experiments.

2.2.5. DNA association and optimization of DNA payload

DNA duplexes assembled with or without Alexa Fluor 488 were mixed with nanoMOFs in aqueous suspension at different DNA amounts of 100 wt%, 30 wt%, 20 wt%, and 10 wt%, calculated as the weight percentage of DNA/nanoMOFs. The adsorption kinetics were performed at 0.5, 1, 2, 4, and 8 h. After each time point, the samples were centrifuged at 10,000 g for 10 min to sediment the nanoMOFs associated with DNA and the free DNA in the supernatant was collected and quantified by UV spectrophotometry (Jenway 7415). The experiments were performed in triplicate.

2.2.6. Association of nanoMOFs with Gem-MP, DS RNA, P-CD-M, and Ad-Rh

NanoMOFs resuspended in water (HyClone, Molecular Biology Grade) at a final concentration of 1 mg/mL were mixed with Gem-MP solutions at a 10:1 mass ratio and then stirred for 4 h to allow Gem-MP to impregnate the nanoMOFs. Afterwards, DS RNA duplexes were added at 10% w/w to the nanoMOFs and incubated at room temperature for 30 min. Then, P-CD-M was added at 10% w/w to the nanoMOFs and the suspension was stirred on a magnetic stir plate for 30 min. As a final step, Ad-Rh was added at 10% w/w to the nanoMOFs and the suspension was stirred for an additional 30 min. Control nanoMOFs were prepared by the same procedure. All samples were freshly prepared the day before the biological experiments.

2.2.7. Characterization methods

The size distribution of nanoMOFs was characterized by dynamic light scattering (DLS; Malvern® Nano-ZS) performed at an angle of 90° and nanoparticle tracking analysis (NTA, LM10 Nanosight, Malvern®). For NTA analysis, the same dilution was used for all the samples and each measurement was repeated 5 times, at room temperature. The particle size distribution was determined using the NTA software. Both

size distribution and particle concentration were obtained by NTA. Transmission electron microscopy (TEM) images of nanoMOFs before and after Gem-MP loading and/or surface modification were collected in a JEOL 1400 transmission electron microscope (TEM, 120 kV, Japan). Zeta potential was determined after diluting the samples using KCl (1 mM).

STEM associated with elemental chemical energy-dispersive X-ray spectroscopy (EDX) cartography was used to evaluate the elemental (C, O, P, Cl and Fe) distribution in the nanoMOFs (Li et al., 2020b). The MIL-100(Fe) nanoMOFs before and after Gem-MP loading and/or surface modification were placed on a copper grid covered with a pure carbon membrane. The STEM observations were made on a Titan Themis 200 microscope (FEI/Thermo Fischer Scientific) equipped with a geometric aberration corrector on the probe. In addition, a "Super-X" system allowed for EDX analysis with a detection angle of 0.9 sr. The observations were made at 200 kV with a probe current of about 50 pA and a half-angle of convergence of 17 mrad. High-angle annular dark-field (HAADF)-STEM images were acquired with a camera length of 110 mm (inner/outer collection angles were respectively 69 mrad and 200 mrad).

Gem-MP quantification was carried out by HPLC (Agilent 1100, USA) using a Phenomenex C_{18} column (4.6 × 250 mm, 5 μm). The mobile phase was composed of 84% buffer (0.2 M triethylamine acetate): 16% methanol and the flow rate was 1.0 mL/min. Gem-MP was detected at 254 nm with an injection volume of 20 μL.

2.2.8. Binding assay

To confirm the binding of nanoMOFs and nucleic acids, Alexa Fluor 488-labeled DNA duplexes were mixed with increasing amounts of nanoMOFs. The final concentration of labeled DNA duplex was maintained at 200 nM in all conditions. The assemblies were incubated at room temperature for 30 min and then visualized on a 2% agarose gel run for 15 min at 200 V in 89 mM tris-borate, 2 mM EDTA. The gel was visualized on a ChemiDoc MP Imaging System (Bio-Rad) for Alexa 488. Alternatively, non-labeled DNA duplexes were used at the same conditions and ethidium bromide total staining was used for their visualization.

2.2.9. Nuclease degradation protection studies

To investigate if binding to nanoMOFs effectively protects the nucleic acid cargo, nanoMOFs were assembled with DNA duplexes carrying a 3' Alexa Fluor 488 and 5' Iowa Black Quencher on separate strands. To the DNA with or without nanoMOFs, 1 μL of RQ1 RNase-Free DNase (Promega) was added in 20 μL reactions which were loaded into a Bio-Rad CFX96 Touch Real-Time PCR Detection System. The DNA amount was kept constant at 1 μM. The temperature was maintained at 37 °C and the relative fluorescence was measured every 30 s for 1 h. As additional controls, DNA duplexes and nanoMOFs were also tested individually. The starting RFU value for each DNase-treated sample was normalized to the non-DNase-treated sample and the differences between each subsequent step were applied to the normalized values. The graph shows the mean of $n = 4$ replicates for each condition ± SEM at each timepoint as the dotted line.

2.2.10. Cell culture

MDA-MB-231 (and GFP expressing MDA-MB-231/eGFP) and HeLa cells were grown in Thermo Scientific Heracell VIOS 160i CO_2 incubators at 37 °C and 5% CO_2. All cells were maintained in DMEM, 10% heat-inactivated fetal bovine serum (Atlanta Biologicals, Inc.), 100 Units/mL penicillin, 100 μg/mL streptomycin (Gibco) throughout all experiments.

2.2.11. Cellular uptake

Twenty-four hours prior to transfection, cells were seeded at 20,000 cells/well in a 12-well plate. Samples were transfected into cells at final concentrations of 250 or 500 nM of fluorescently labeled DNA duplexes

corresponding to 20.8 or 41.7 μg/mL nanoMOFs, respectively, based on their complexed ratios. Uptake was assessed after 48 h. Cells were washed with PBS and visualized using an EVOS FL microscope for GFP (using a GFP light cube with 482/25 Ex; 524/24 Em) and Ad-Rh (using a Cy5 light cube with 628/40 nm Ex; 692/40 Em).

2.2.12. GFP silencing

Twenty-four hours prior to transfection, MDA-MB-231/eGFP cells were seeded at 40,000 cells/well in a 12-well plate. Samples were transfected into cells at final concentrations of 50, 100, or 250 nM DS RNA corresponding to 4.2, 8.3, or 20.8 μg/mL nanoMOFs, respectively, based on their complexed ratios. GFP silencing was assessed after 48 h. Cells were washed with PBS and incubated with Trypsin-EDTA (0.25%, Gibco) for 5 min at 37 °C, 5% CO_2 for detachment. Media was added and the resuspended cells were then centrifuged at 300 g for 5 min twice, following PBS washes. Afterwards, the cell pellets were redispersed in 10% neutral-buffered formalin for 15 min at room temperature, followed by another centrifugation at 300 g for 5 min. Cell pellets were resuspended in PBS for analysis using a BD Accuri C6 flow cytometer equipped with a blue (488 nm) laser and 533/30 optical filters. Cells-only were used to gate 10,000 events per sample for collection.

2.2.13. Cell toxicity

Twenty-four hours prior to transfection, MDA-MB-231 cells were seeded at 10,000 cells/well in a 96-well plate. Samples were transfected into cells at a final concentration of 750 nM DS RNA corresponding to 62.5 μg/mL nanoMOFs, respectively, based on their complexed ratios. Toxicity was assessed after 72 h using a CellTiter 96® AQ$_{ueous}$ One Solution Cell Proliferation Assay (MTS). Then, 20 μL of reagent was added to each well and was incubated for 75 min at 37 °C, 5% CO_2 prior to reading the absorbance at 490 nm on a Tecan Spark plate reader.

2.2.14. Statistical analysis

All graphs with statistical analysis were prepared using GraphPad Prism version 9.0.0 for Windows, GraphPad Software, San Diego, California, USA, www.graphpad.com. Figures were prepared using Adobe Illustrator 24.0.2 (64-bit).

3. Results & discussion

3.1. NanoMOFs' synthesis and DNA duplexes' association

Porous MIL-100(Fe) nanoMOFs with BET (Brunauer, Emmett, and Teller) surface areas of 1450 ± 50 m^2 g^{-1} were successfully prepared by an organic solvent-free "green" hydrothermal method (Fig. 1A). The synthesized nanoMOFs exhibited a facetted morphology (Fig. 1B) as previously reported (Agostoni et al., 2015). High resolution STEM investigations clearly evidenced their crystalline structures with regular planes (Fig. 1C).

The size distribution of the synthesized nanoMOFs was characterized by both DLS and NTA. As shown in Fig. S1A, no significant difference was found in terms of mean diameters (127 ± 14 nm, PDI = 0.1, by DLS, and 130 ± 44 nm by NTA). DNA duplexes were firstly used as a cost-efficient nucleic acid model to optimize binding to the nanoMOFs.

MIL-100(Fe) nanoMOFs possess two types of mesoporous cages: small cages (free diameter ~24 Å) delimited by pentagonal windows (~5 Å) and large cages (free diameter ~27 Å) accessible also through hexagonal windows (~9 Å) (Fig. 1A) (Horcajada et al., 2009). DNA duplexes are too bulky to penetrate within the pores, thus they are prone to localize only on the nanoMOF's external surface. Furthermore, the phosphate moieties of DNA duplexes could readily interact with iron sites at the nanoMOF's surface, as it was shown with other phosphorylated (macro)molecules (Agostoni et al., 2015; Rodriguez-Ruiz et al., 2015; Christodoulou et al., 2021; Li et al., 2017). Fig. S2A displays the fast binding of DNA duplexes and nanoMOFs within 30 min, quite probably caused by strong coordination between the phosphate moieties of DNA and the nanoMOFs' Fe sites. The maximal DNA amount associated to nanoMOFs was up to 33 ± 6 wt% when DNA was added at 100% w/w to the nanoMOFs.

An almost perfect association efficiency (close to 100%) was achieved when DNA was added at 10% w/w to the nanoMOFs. However, under this condition, an evident aggregation was observed immediately
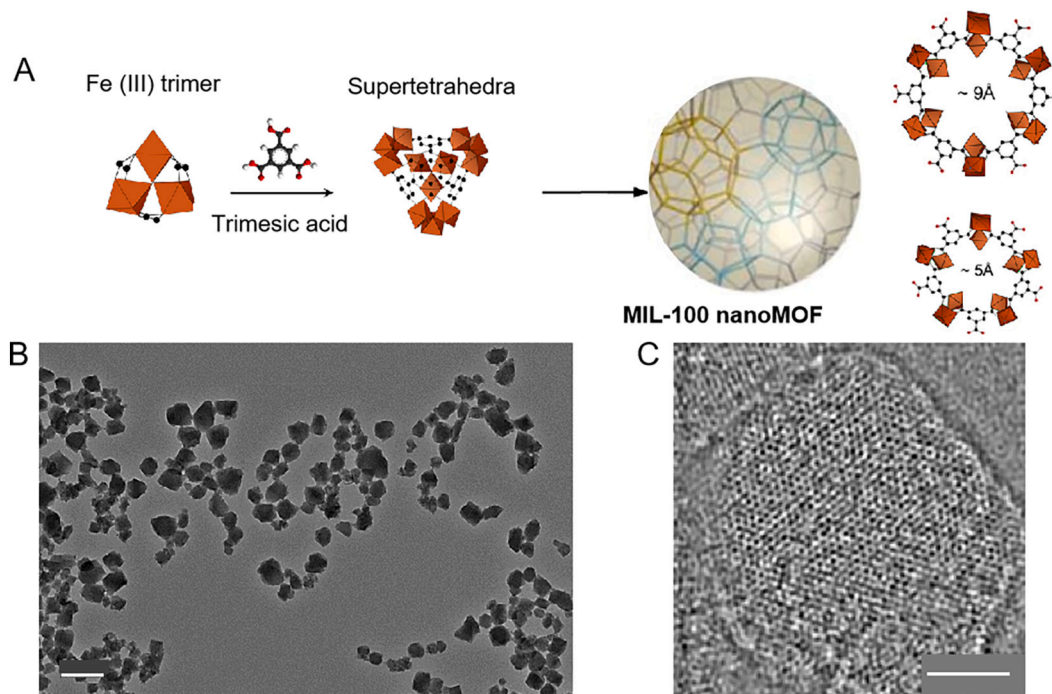

Fig. 1. (A) Schematic representation of MIL-100(Fe) nanoMOFs' synthesis by the assembly of iron trimers and trimesic acid, forming an open porous structure with large and small cages with diameters of around 9 and 5 Å, respectively. (B) TEM image of nanoMOFs (scale bar: 200 nm) and (C) a close-up by STEM (scale bar: 40 nm).

after mixing DNA duplexes and nanoMOFs (the mean diameter of the complexes was >1 μm, Fig. S2B). This could be explained by the possible bridging effect of DNA duplexes in reason of their high affinity for the nanoMOFs. However, at higher amounts of DNA in contact with the nanoMOFs (when DNA was added at ≥20% w/w to the nanoMOFs), no aggregation was observed. Furthermore, the presence of DNA duplexes on the external nanoMOFs' surfaces was strongly suggested by the Zeta potential shift from +28 ± 5 mV (bare nanoMOFs) to −42 ± 3 mV (after DNA binding) attributed to the introduction of negatively charged DNA macromolecules.

To expand the versatility of our new combinatorial system, we introduced Gem-MP as an additional therapeutic agent following the procedures described in our previous reports (Rodriguez-Ruiz et al., 2015). Interestingly, when Gem-MP (10 wt%) was incorporated inside the pores of nanoMOFs with almost perfect loading efficiency (>98%), it did not significantly influence the efficiency of DNA association, size distribution, and Zeta potential (variation less than 10%) of the resulting nanoMOF complexes (Fig. S2).

In order to target cancer cells that abundantly-express the mannose receptor (Lin et al., 2020), the nanoMOF's surface was modified with mannose-bearing coatings, as described in our previous strategy (Cutrone et al., 2019a). Briefly, phosphate cyclodextrin mannose (P-CD-M) was successfully synthesized, where the phosphate moieties are designed to anchor to the surface of nanoMOFs and mannose ligands to target cancer cells. Rapid anchoring was observed within 30 min, leading to an efficient and stable surface modification of the nanoMOFs. As in our previous report (Cutrone et al., 2019a), surface functionalization did not modify the nanoMOF size distribution (variation less than 10%).

Finally, to track the internalization of the surface modified nano-MOFs by confocal microscopy and flow cytometry, adamantane-rhodamine (Ad-Rh) was synthesized to label the nanoMOFs (Li et al., 2020a). We demonstrated that Ad-Rh was efficiently associated to the surface of nanoMOFs, reaching 8.2 ± 0.2 wt%, and was only slightly released (<10%) after incubation at 37 °C for 6 h in cell culture medium (Li et al., 2020a). Again, this surface functionalization did not modify the nanoMOF size distribution (variation less than 10%).

In this study, we combined both coating and labelling strategies (Ad-Rh and P-CD-M) to elaborate multifunctional composites to co-deliver both small anticancer drugs (Gem-MP) and macromolecules (TNAs).

3.1.1. STEM-EDX characterization

To characterize in-depth the DNA-loaded targeted delivery system, we employed scanning transmission electron microscopy (STEM) coupled with elemental chemical energy-dispersive X-ray spectroscopy (EDX) cartography to visualize the nanoMOFs and determine their elemental composition. All elements in the nanoMOFs were clearly identified, including "Fe," "Cl," (Fig. 2A) "C," and "O" (Fig. S3). As expected, no "P" was observed in as-synthesized nanoMOFs. After interaction with DNA duplexes, the "P" signal characteristic of DNA appeared and co-localized with the "Fe" one, corresponding to the MIL-100(Fe) nanoMOFs. Notably, no "P" signal was observed on the grids, suggesting the DNA duplexes specifically associated to the nanoMOFs. Similar results were found with nanoMOFs coated with P-CD-M, loaded or not
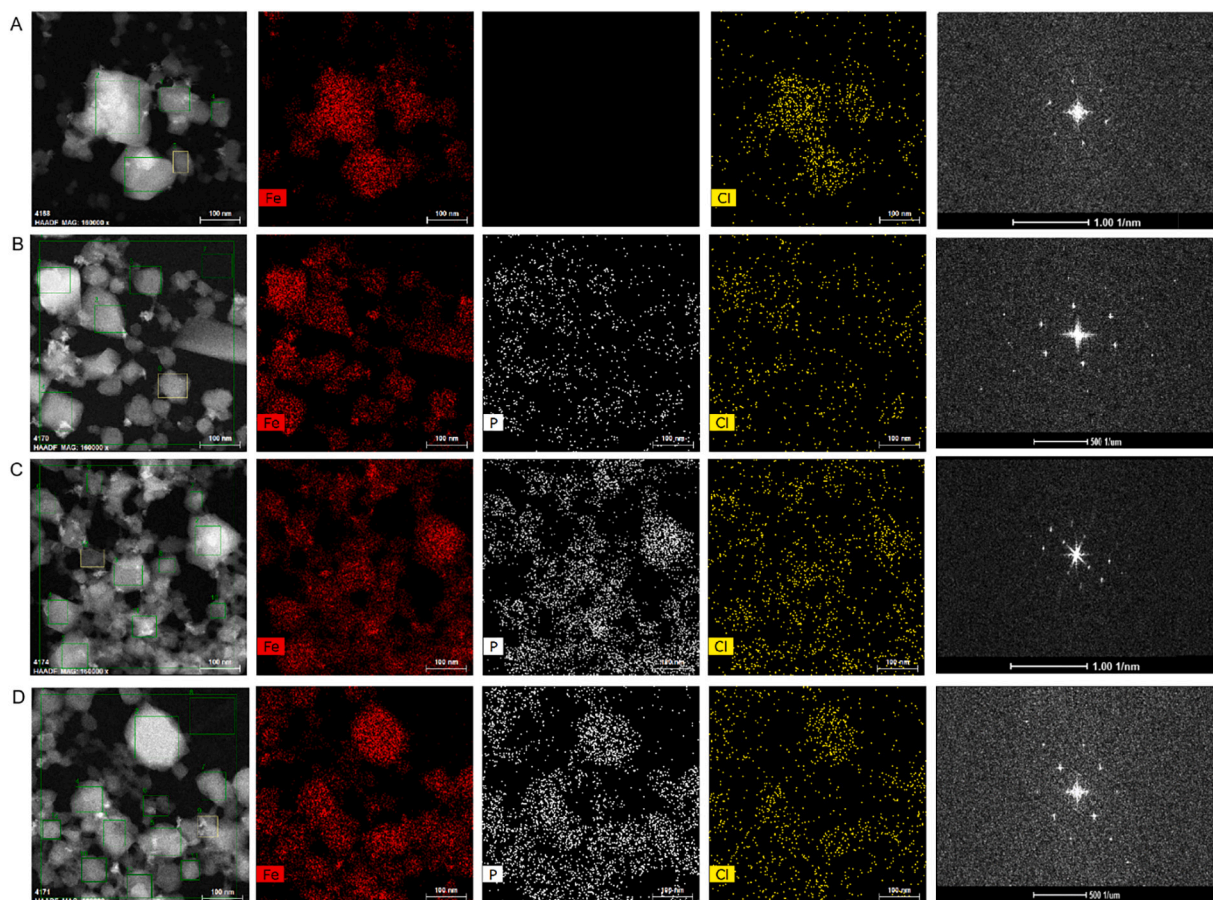

Fig. 2. Microscopic observation of nanoMOF samples. Morphology of nanoMOFs and STEM images (left panel) together with EDX mapping (three middle panels) and Fourier Transform pattern of an HAADF-STEM image of a single crystal nanoMOF (right panel) of (A) empty nanoMOFs, (B) DNA@nanoMOFs 20 wt%, (C) P-CD-M@nanoMOFs 10 wt%, and (D) DNA@P-CD-M@nanoMOFs. The green rectangles in the left four panels indicate the selected regions of interest used to calculate the P/Fe molar ratios (reported in the supporting information). (For interpretation of the references to colour in this figure legend, the reader is referred to the web version of this article.)

with DNA (Fig. 2C-D).

To gain additional understanding of the homogeneity of the nano-MOFs' composition, nanoparticles were randomly chosen from each formulation (empty nanoMOFs, DNA@nanoMOFs 20 wt%, P-CD-M@nanoMOFs 10 wt%, and DNA@P-CD-M@nanoMOFs) to calculate the molar ratio P/Fe from EDX mapping. Fig. S4 summarizes the results obtained from the investigation of twelve nanoMOFs, focusing on the molar ratio P/Fe, an indicator of the associated DNA and/or P-CD-M amount. It was found that the ratio P/Fe is related to the nanoMOF size: the larger the particle size, the lower their P/Fe value. This suggests a preferential location of DNA onto the nanoMOFs' surface. In addition, Fig. S5 displays the P/Fe molar ratio of DNA@P-CD-M@nanoMOFs composites. The results suggest that the amount of DNA and P-CD-M in DNA@P-CD-M@nanoMOFs practically corresponds to the amounts of DNA and P-CD-M in individual DNA@nanoMOFs and P-CD-M@nano-MOFs. These results are in agreement with the strong interactions between the nanoMOFs and both DNA and P-CD-M. Furthermore, the presence of P-CD-M did not interfere with the DNA loading. This was confirmed by DNA quantification by UV spectroscopy, showing little DNA loading differences before and after surface modification with P-CD-M (15 wt% and 13 wt%, respectively). Noteworthy, the organized supramolecular structure of the nanoMOFs was preserved after DNA association and surface modification with P-CD-M (Fourier Transform patterns of the HAADF-STEM images of randomly chosen nanoMOFs, Fig. 2).

3.1.2. NTA analyses

In complement to STEM investigations, NTA analysis brought new insights on the colloidal stability of DNA@P-CD-M@nanoMOFs composites (Table 1). Nanoparticle size distribution is commonly determined by DLS. In addition to DLS we used NTA, which combines a conventional optical microscope with a laser to illuminate nanoMOFs in Brownian motion. NanoMOFs scattered light and were thus visualized one by one as moving points (Fig. S1B). This allowed determining both nanoMOFs' size distribution and concentration, before and after nucleic acids loading and/or surface modifications. Advantageously, the fluorescent nanoMOFs (labeled with Rh) could be also specifically tracked by using a fluorescence filter, thus allowing determining their mean hydrodynamic diameter and concentration.

In short, the nanoMOFs were characterized to measure their mean size and concentration by two independent methods, with and without

fluorescence filter. This allowed gaining knowledge about the respective concentrations of labeled and non-labeled nanoMOFs, as a quality control of the formulations.

We observed that adding DNA at 20% w/w of the nanoMOFs did not significantly modify their mean diameters nor their concentration (130 $\pm$ 44 nm, $2.38 \times 10^9 \pm 5.8 \times 10^7$ particles/mL and 134 $\pm$ 55 nm, $2.43 \times 10^9 \pm 1.4 \times 10^7$ particles/mL for nanoMOFs before and after DNA association, respectively). The results were in good agreement with the DLS data (Fig. S2B), indicating that no aggregation occurred during DNA association. However, when excess DNA duplexes were added to the nanoMOFs (1:1 weight ratio), the mean diameter decreased from 130 $\pm$ 44 nm to 96 $\pm$ 26 nm, whereas the particle concentration increased from $2.38 \times 10^9 \pm 5.8 \times 10^7$ particles/mL to $3.79 \times 10^9 \pm 1.4 \times 10^8$ particles/mL.

Interestingly, when the nanoMOFs were associated with both DNA and P-CD-M (20 wt% DNA and 10 wt% P-CD-M), no aggregation was observed. Moreover, Table 1 shows that the mean diameter and particle concentration only slightly decreased. In addition, when the nanoMOFs were labeled with Ad-Rh, the mean hydrodynamic diameters were not affected and only a slight decrease in particle concentration was observed when tracking either nanoMOFs or Ad-Rh-nanoMOFs. This offers direct evidence that almost every nanoMOF particle was well labeled. The decrease in particle concentration between unlabelled and Rh-labeled nanoMOFs could possibly be explained by the fact that a tiny fraction of the smallest labeled nanoMOFs are too dim to be detected, as previously reported (Bourguignon et al., 2021; Pancani et al., 2018). It is worth noting that Ad-Rh could efficiently self-assemble with P-CD-M by the "host-guest" interaction between "Ad" and "β-CD" (Wang et al., 2021). Similarly, no significant size variation was observed for the DNA-P-CD-M-Ad-Rh-nanoMOFs composites in comparison to empty nano-MOFs, confirming that the DNA loading and surface modification did not induce aggregation and the nanoMOF particles were well labeled by fluorescent moieties allowing for further tracking in cells. To summarize, the nanoMOFs spontaneously associated with DNA duplexes and coating materials on their surfaces, without inducing aggregation.

3.2. Binding of fluorescently labeled DNAs to nanoMOFs and protection of nucleic acid cargo from nuclease degradation

To provide an additional tool for DNA:nanoMOFs binding assessment and tracking of resulting nanoparticles in biological environment, DNA duplexes fluorescently labeled with Alexa Fluor 488 (Al488) were associated to the nanoMOFs. The amount of labeled DNA duplexes was kept constant while the amount of nanoMOFs was increased to investigate their binding process. The samples were analyzed by an electrophoretic mobility shift assay as shown in Fig. 3A in which binding of the fluorescently labeled DNA duplexes resulted in a shift of the corresponding fluorescence band to the bottom of the gel due to the formation of larger complexes. Alternatively, non-labeled DNA duplexes were run using the same conditions. The agarose gel was stained with ethidium bromide (EtBr) and visualized to further confirm the DNA binding to nanoMOFs (Fig. S6). First, an incomplete binding was observed at a DNA:nanoMOF ratio of 1:50, with full binding observed at a 1:100 ratio. In the light of these findings, to ensure all nucleic acids are bound, the 1:200 ratio was used throughout all subsequent studies.

Then, the protective capabilities of the DNA:nanoMOF complexes against nucleases were tested. Previous studies have shown that siRNAs associated to the surface of nanoparticles results in enzymatic degradation upon exposure to serum (Barnaby et al., 2014). To address this concern, we used here a nuclease protection assay set up in previous investigations (Avila et al., 2021; Halman et al., 2020; Kim et al., 2020; Nordmeier et al., 2020; Juneja et al., 2020) was utilized. The assay used DNA duplexes containing 5' Iowa Black Quencher and 3' Al488 on complementary strands which were then complexed with the nanoMOF (1:200) and then treated with RQ1 DNase.

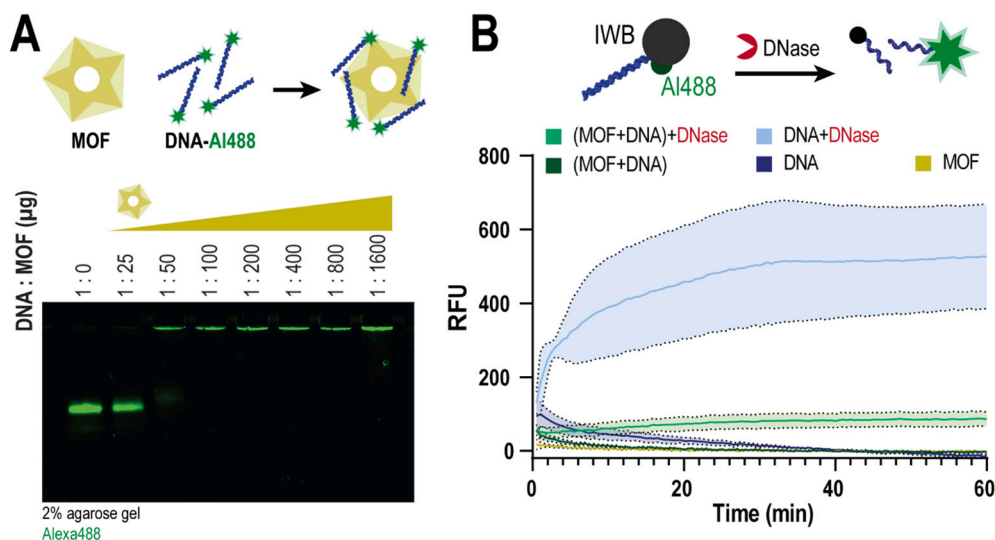Both the nanoMOF complexed and non-complexed DNA duplexes

Table 1
Mean hydrodynamic diameter and particle concentration from NTA measurement of nanoMOFs before and after DNA loading and surface modification. Two NTA modalities were used, to track the whole nanoMOF population or only fluorescent nanoMOFs.

Sample	DLS measurement		NTA analysis	
	Z-average (nm)	PDI	Mean D_h (nm)	Concentration (particle/mL)
Empty nanoMOFs	127 ± 14	0.09	130 ± 44	$2.38 \times 10^9 \pm 5.8 \times 10^7$
DNA-nanoMOFs 20 wt%	128 ± 10	0.12	134 ± 55	$2.43 \times 10^9 \pm 1.4 \times 10^7$
DNA-nanoMOFs 100 wt%	125 ± 11	0.20	96 ± 26	$3.79 \times 10^9 \pm 1.4 \times 10^8$
DNA-P-CD-M@nanoMOFs	141 ± 11	0.23	108 ± 26	$2.19 \times 10^9 \pm 8.4 \times 10^7$
Ad-Rh-nanoMOFs (tracking nanoMOFs)	132 ± 16	0.24	113 ± 26	$2.69 \times 10^9 \pm 3.9 \times 10^7$
Ad-Rh-nanoMOFs (tracking Rh)			121 ± 29	$2.18 \times 10^9 \pm 4.1 \times 10^7$
DNA-P-CD-M-Ad-Rh-nanoMOFs (tracking nanoMOFs)	139 ± 14	0.21	127 ± 31	$2.31 \times 10^9 \pm 6.2 \times 10^7$
DNA-P-CD-M-Ad-Rh-nanoMOFs (tracking Rh)	145 ± 13	0.25	138 ± 53	$1.95 \times 10^9 \pm 4.9 \times 10^7$

Fig. 3. Binding of DNA duplexes to nanoMOFs and nuclease protection of nucleic acid cargo. (A) Schematic illustrating the DNA-nanoMOF assembly. The binding of Al488-labeled DNA duplexes to nanoMOFs is assessed by an electrophoretic mobility shift assay. (B) Subsequently, binding to the nanoMOF protects DNA duplexes from nuclease degradation over one hour. Separation of the fluorophore/quencher pair upon nuclease degradation results in increased fluorescence.

were studied in the presence of RQ1 DNase. Upon nuclease degradation of the unprotected duplexes, the separation of the quencher and fluorophore pair resulted in an increased fluorescence from the DNase-treated DNA over an hour, which was around five times higher than in the case of nanoMOF-bound DNA (Fig. 3B). The absence of significant fluorescence from the Al488 DNA duplex complexed to nanoMOFs indicates that the Iowa Black Quencher continued to quench the Al488 fluorescence because of the proximity of both strands, meaning that the addition of RQ1 DNase to the DNA:nanoMOF complexes did not result in the degradation of the duplexes. Moreover, the nanoMOFs protected the DNA duplexes against degradation for up to five hours (Fig. S7), showing that complexation to the nanoMOF provides stability and protection from nuclease degradation.

3.3. Cellular co-uptake of fluorescently labeled nanoMOFs and DNA duplexes

Here, nanoMOFs were used to investigate the delivery of fluorescently labeled DNA duplexes. The nanoMOFs were also functionalized with coatings and fluorescent moieties (Ad-Rh and P-CD-M) in an attempt to increase their interaction with cancer cells, and in order to visualize them by confocal microscopy.

The uptake of DNA:nanoMOF complexes was first observed upon their transfections into the MDA-MB-231 (human breast cancer) cell line, and then confirmed in the HeLa (human cervical cancer) cell line (Fig. S8). In addition to DNA-Al488, P-CD-M was associated to the nanoMOFs in an attempt to increase their targeting potential for mannose receptors overexpressed in MDA-MB-231 cancer cell lines (Lin et al., 2020).

To track the uptake of the complexed nanoMOFs, they were tagged with Ad-Rh as in previous studies (Li et al., 2020a, 2020b, 2020c) ensuring stability in biological media (Fig. 4A). After 48 h, the uptake of all complexes was assessed *via* fluorescence microscopy (Fig. 4B). DNA-Al488 delivered with nanoMOFs (shown in GFP panels) and DNA delivered with Ad-Rh nanoMOFs (shown in Ad-Rh panels) show the respective fluorescence of each component in cells (shown in the brightfield panels). The functionalized DNA-Al488/Ad-Rh nanoMOFs were taken up by the cells both with and without the addition of P-CD-M. Additional microscopy data of the uptake experiments in HeLa and MDA-MB-231 cells are available in the Supporting Information (Fig. S9–10). From the microscopy images in Fig. 4, it can be observed that fluorescence from Al488 and Ad-Rh co-localises. The confocal

images show that both the nanoMOFs and the fluorescently labeled DNA duplex are internalized into the cells. Interestingly, the addition of P-CD-M did not increase the internalization of the complexes into cells, as expected and seen in (Lin et al., 2020) when using mannose as a functionality to their nanocarrier into MDA-MB-231 cells. In addition, previous studies with P-CD-M functionalized MIL-100(Fe) nanoMOFs showed that they were efficiently internalized in human retinoblastoma Y79 cell line (Agostoni et al., 2015). More investigations will be necessary to determine why the functionalized nanoMOFs were not able to increase the uptake in MDA-MB-231 cells.

3.4. NanoMOFs loaded with RNAi inducers are functional in cells

To test the intracellular delivery and release of functional RNAs in MDA-MB-231 cells gene silencing experiments were carried out for nanoMOFs complexed with Dicer Substrate (DS) RNAs designed to target GFP (Rose et al., 2005). Once delivered into the cytoplasm, DS RNAs undergo intracellular Dicer-assisted release of siRNAs that induce RNAi-mediated downregulation of target protein expression (Rose et al., 2005). DS RNA-loaded nanoMOFs were also complexed with P-CD-M to test whether the addition of this functional surface moiety could increase their uptake. Like in the previous studies, the nanoMOFs were also labeled with Rh to allow their visualization by confocal microscopy (Fig. 5A). The nanoMOF complexes were tested in the human breast cancer cell line MDA-MB-231 stably expressing GFP. Microscopy images show the expression of GFP from untreated cells. Rh-labeled RNA-MOFs were first introduced into the cell line with DS RNAs designed to knockdown GFP (GFP DS RNAs). After 48 h, the nanoMOFs are visible in cells, which is evident in the Ad-Rh panels, with some level of GFP knockdown observed as indicated by a visual decrease in the fluorescence microscopy images. However, with the addition of the P-CD-M targeting agent, the Ad-Rh signal appears brighter, signifying a higher presence of nanoMOFs in the cells, while the GFP knockdown appears to be more efficient because of the visual decrease in fluorescence associated with GFP. In order to confirm these findings, and quantify the nanoMOF-cell interactions, we used flow cytometry to analyze the cells transfected with different concentrations of GFP DS RNAs (50, 100, and 250 nM), complexed with nanoMOFs in a 1:200 ratio (Fig. 5C). As a control, the same concentrations of GFP DS RNAs were delivered using Lipofectamine 2000 (L2K), a commercially available lipid-based carrier. At 250 nM GFP DS RNAs, the P-CD-M targeted RNA-nanoMOFs showed statistically significant ($P < 0.0001$) knockdown compared to the cells-
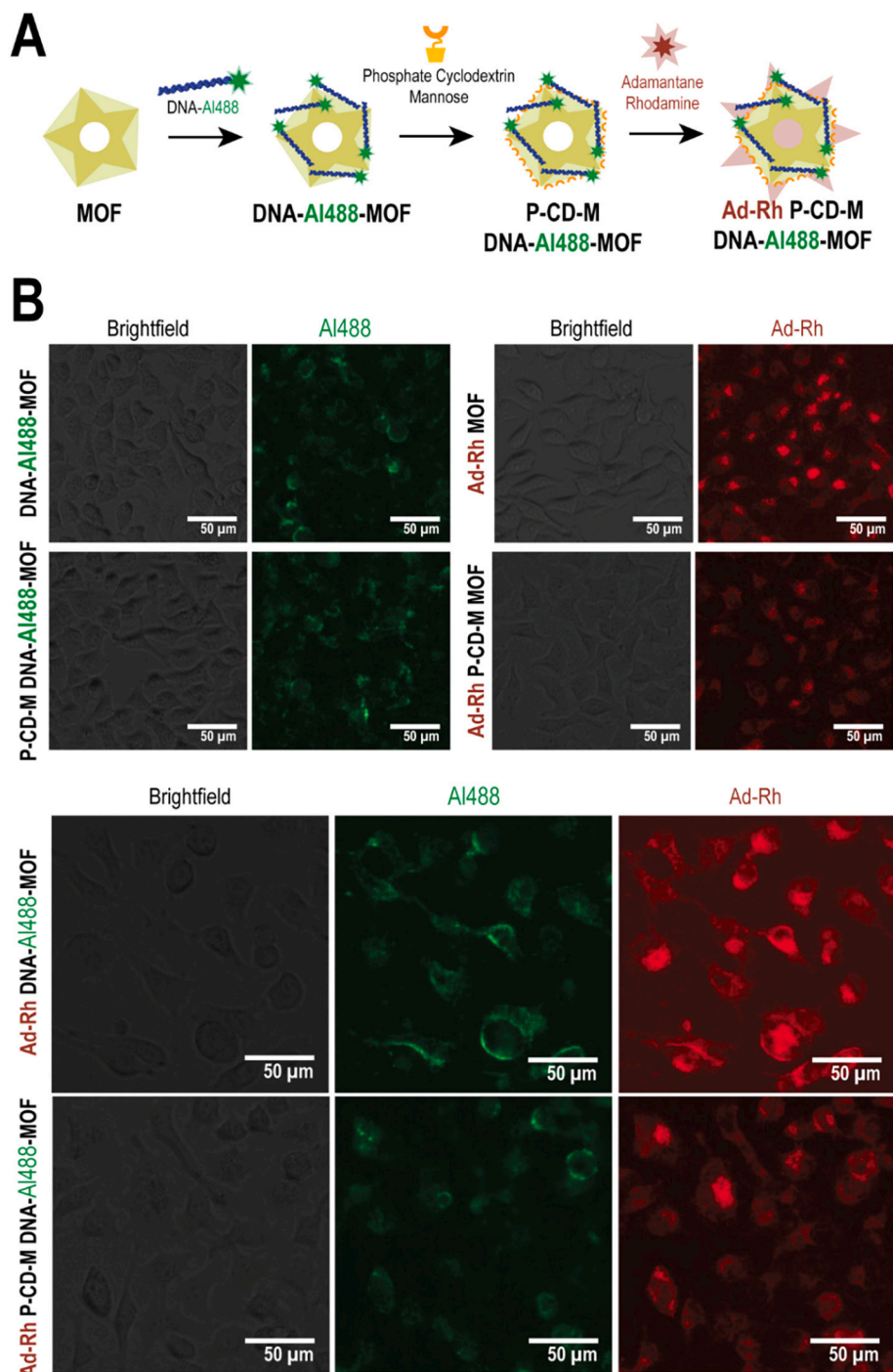
Fig. 4. Complexation of nanoMOFs with DNA-Al488, P-CD-M, and Ad-Rh for uptake in HeLa cells. (A) Schematic illustrating the stepwise assembly of nanoMOF complexes for the cellular uptake experiments. (B) Fluorescence microscopy of Al488-DNA and Ad-Rh nanoMOFs in HeLa cells 48 h post-transfection. Cells were seeded at 20,000 cells per well and transfected with 500 nM DNA-Al488 or respective concentrations of nanoMOFs. Scale bar = 50 μm.

only control, which was comparable to the L2K control of the same concentration. In comparison, the non-targeted RNA-nanoMOFs showed no significant knockdown.

3.5. Targeted multimodal toxicity of nanoMOFs and TNAs in cancer cells

Due to their highly porous structure, nanoMOFs can be efficiently loaded with therapeutic drugs for their delivery and release over time in the cellular environment. To take advantage of this capability, the nanoMOFs were further engineered for combinatorial therapeutic

activity. To do so, they were loaded with Gem-MP prior to their complexation with DS RNAs, and the resulting RNA-Gem-MP-nanoMOFs were further decorated with P-CD-M (Fig. 6A). Various concentrations for each individual component of tested formulations and their effects on cell viability were assessed (Figs. S11–12). The concentrations of nanoMOFs used for all toxicity experiments were selected based on the non-toxic effects of the materials alone. Here, nanoMOFs were complexed with DS RNAs against Survivin (Surv DS RNA), an inhibitor of apoptosis, wherein knockdown of this gene will result in a promotion of apoptosis, or a decrease in cell viability (Wang et al., 2020). Upon
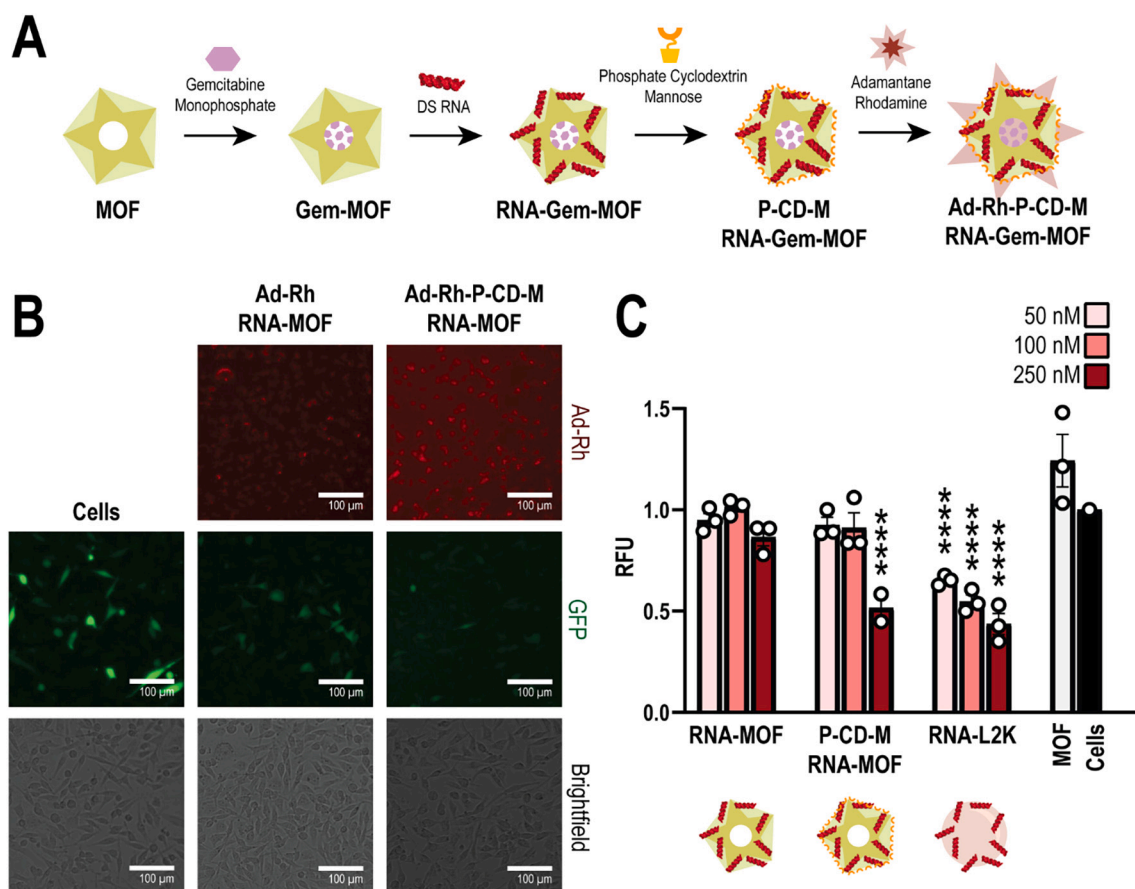
Fig. 5. Complexation of nanoMOFs with GFP DS RNAs, P-CD-M, and Ad-Rh for specific gene silencing in cancer cell lines measured 48 h after. (A) Schematic demonstrating the stepwise assembly of nanoMOF complexes. (B) Silencing of GFP by targeted P-CD-M nanoMOF complexes in MDA-MB-231 GFP cells. 250 nM GFP DS RNAs is shown in both cases. Scale bar = 100 μm. (C) Silencing activity of targeted nanoMOFs in MDA-MB-231 eGFP cells compared to L2K control. Three different concentrations of DS RNAs were tested, all delivered at a 1:200 ratio with nanoMOF. RFU was normalized to untreated cells and nanoMOFs alone are shown as a control. Bars denote mean ± SEM of $n = 3$ repeats. Statistical significance to the untreated cells was determined by a two-way ANOVA and is denoted with asterisks (**** P-value <0.0001).

delivery of the nanoMOF-Surv DS RNA there was a slight decrease in cell viability. However, upon addition of Gem-MP and P-CD-M to the nanoMOFs, the combinatorial therapy resulted in significant decreases in cell viability ($P < 0.01$ and $P < 0.001$, respectively) (Fig. 6B).

Based on the results of the toxicity experiments, it appears that P-CD-M did not enhance the therapeutic effects of the RNA-Gem-MOF combination. However, the results from these studies show that upon loading the nanoMOFs with Gem-MP, there is a significant difference in the therapeutic efficacy of the Surv DS RNA nanoMOF combination. This finding suggests that the nanoMOFs successfully co-delivered both therapeutic agents to enact a combinatorial therapeutic effect.

4. Conclusions

Engineered nanoMOFs effectively delivered TNAs into cancer cells. This was observed with uptake experiments into cancer cells using fluorescently labeled DNAs and was further validated by the significant knockdown of GFP in the GFP-expressing MDA-MB-231 breast cancer cells *via* RNA interference. We further explored the efficacy of nanoMOFs decorated with TNAs, Ad-Rh and P-CD-M. Surprisingly, mannosylation with P-CD-M did not provide an increased therapeutic effect and will require further investigation of the nanoMOF uptake mechanism in different cancer cell lines.

As shown by nuclease protection assays, nanoMOFs protect their nucleic acid cargo from enzymatic degradation. Additionally, nanoMOFs efficiently co-delivered therapeutic DS RNAs and Gem-MP. The combination of these two therapeutic agents provided an enhanced therapeutic effect. This finding is consistent with previous reports of combined therapeutic strategies. For example, MOFs have been used to co-deliver cisplatin and siRNAs to ovarian cancer cells and were shown to protect against nuclease degradation while increasing cellular uptake (He et al., 2014). Other strategies using gemcitabine and TNAs co-delivered in polymeric nanoplatforms have been shown for targeted delivery into tumor cells while minimizing off-target toxicity (Xin et al., 2020; Zhang et al., 2013). Gemcitabine has also been combined with other therapeutics, such as MUC1 inhibitors, for co-delivery *via* co-polymers into breast cancer cells which showed greater efficacy than when delivered separately (Grossen et al., 2017).

Nevertheless, while these strategies demonstrate both the feasibility and flexibility to fine-tune these nanoMOF materials, additional studies are needed to build upon the current platform. Future work will be required to explore nanoMOF's potential to deliver larger TNAs and nucleic acid complexes in conjunction with other anticancer therapeutics into cells. There is also potential to integrate these versatile nanoMOFs into higher ordered three-dimensional structures by using programmable nucleic acids (Chandler et al., 2021; Chandler et al., 2022).

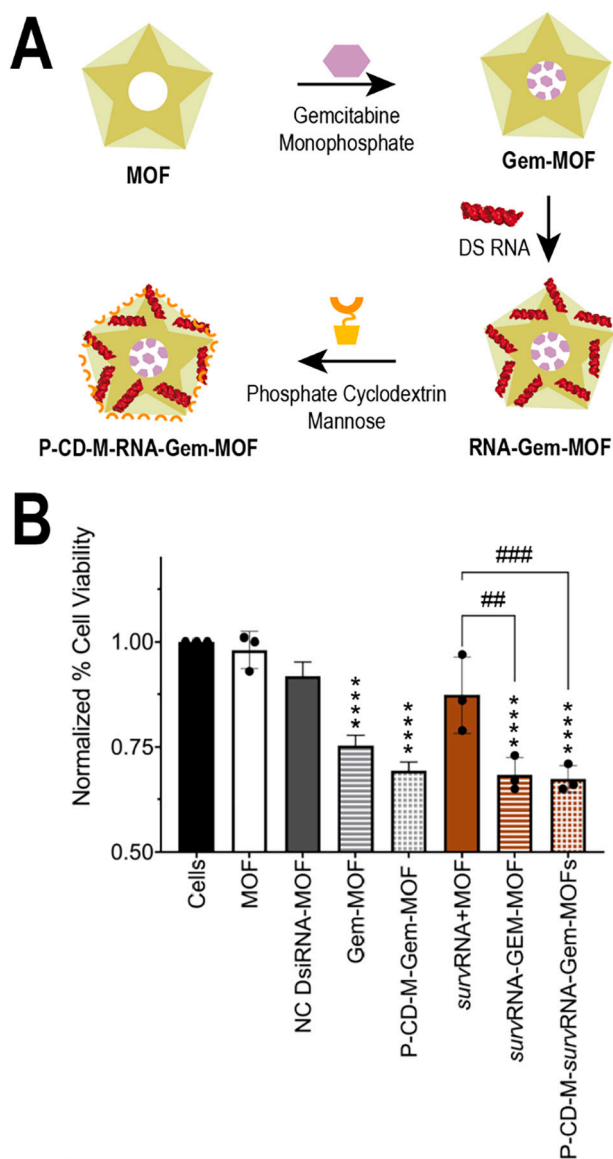## Declaration of Competing Interest

None.

Fig. 6. Toxicity of Gem-MP and DS RNA nanoMOFs. (A) Schematic illustrating the stepwise assembly of nanoMOF complexes for toxicity experiments. (B) Normalized % cell viability by targeted nanoMOF complexes in MDA-MB-231/ eGFP cells. Cells were seeded at 10,000 cells/well and assessed after 72 h. Cell viability was normalized to untreated cells and bars denote mean ± SD of $n = 3$ repeats. Horizontal stripes denote Gem-MP and vertical stripes denote P-CD-M. [nanoMOFs] is 62.5 µg/mL in all conditions for 750 nM [DS RNA]. A one-way ANOVA was used to determine statistical significance: significance to the untreated cells is denoted with asterisks (**** P-value <0.0001) and significance of the addition of Gem-MP and P-CD-M to each RNA-nanoMOF is denoted with pound signs (## P-value <0.01, ### P-value <0.001) A scrambled sequence (DsiRNA) is included as an additional control.

Data availability

Data will be made available on request.

Acknowledgements

Appendix A. Supplementary data

Supplementary data to this article can be found online at https://doi.org/10.1016/j.ijpx.2023.100161.

References

Agostoni, V., Chalati, T., Horcajada, P., Willaime, H., Anand, R., Semiramoth, N., Baati, T., Hall, S., Maurin, G., Chacun, H., Bouchemal, K., Martineau, C., Taulelle, F., Couvreur, P., Rogez-Kreuz, C., Clayette, P., Monti, S., Serre, C., Gref, R., 2013. Towards an improved anti-HIV activity of NRTI via metal-organic frameworks nanoparticles. Adv. Healthc. Mater. 2, 1630–1637. https://doi.org/10.1002/adhm.201200454.
Agostoni, V., Horcajada, P., Noiray, M., Malanga, M., Aykaç, A., Jicsinszky, L., Vargas-Berenguel, A., Semiramoth, N., Daoud-Mahammed, S., Nicolas, V., Martineau, C., Taulelle, F., Vigneron, J., Etcheberry, A., Serre, C., Gref, R., 2015. A "green" strategy to construct non-covalent, stable and bioactive coatings on porous MOF nanoparticles. Sci. Rep. 5, 7925. https://doi.org/10.1038/srep07925.
Avila, Y.I., Chandler, M., Cedrone, E., Newton, H.S., Richardson, M., Xu, J., Clogston, J.D., Liptrott, N.J., Afonin, K.A., Dobrovolskaia, M.A., 2021. Induction of cytokines by nucleic acid nanoparticles (NANPs) depends on the type of delivery carrier. Molecules 26, 652. https://doi.org/10.3390/molecules26030652.
Baati, T., Njim, L., Neffati, F., Kerkeni, A., Bouttemi, M., Gref, R., Najjar, M., Zakhama, A., Couvreur, P., Serre, C., Horcajada, P., 2013. In depth analysis of the in vivo toxicity of nanoparticles of porous iron(iii) metal–organic frameworks. Chem. Sci. 4, 1597–1607. https://doi.org/10.1039/c3sc22116d.
Barnaby, S.N., Lee, A., Mirkin, C.A., 2014. Probing the inherent stability of siRNA immobilized on nanoparticle constructs. PNAS 111, 9739–9744. https://doi.org/10.1073/pnas.1409431111.
Bellido, E., Hidalgo, T., Lozano, M.V., Guillevic, M., Simón-Vázquez, R., Santander-Ortega, M., González-Fernández, A., Serre, C., Alonso, M.J., Horcajada, P., 2015. Heparin-engineered mesoporous iron metal-organic framework nanoparticles: toward stealth drug nanocarriers. Adv. Healthc. Mater. 4, 1246–1257. https://doi.org/10.1002/adhm.201400755.
Bourguignon, T., Torrano, A.A., Houel-Renault, L., Machelart, A., Brodin, P., Gref, R., 2021. An original methodology to study polymeric nanoparticle-macrophage interactions: nanoparticle tracking analysis in cell culture media and quantification of the internalized objects. Int. J. Pharmaceut. 610, 121202 https://doi.org/10.1016/j.ijpharm.2021.121202.
Chandler, M., Minevich, B., Roark, B., Viard, M., Johnson, M.B., Rizvi, M.H., Deaton, T.A., Kozlov, S., Panigaj, M., Tracy, J.B., Yingling, Y.G., Gang, O., Afonin, K.A., 2021. Controlled organization of inorganic materials using biological molecules for activating therapeutic functionalities. ACS Appl. Mater. Interfaces 13, 39030–39041. https://doi.org/10.1021/acsami.1c09230.
Chandler, M., Rolband, L., Johnson, M.B., Shi, D., Avila, Y.I., Beasock, D., Danai, L., Stassenko, E., Krueger, J., Jiang, J., Lee, J.S., Dobrovolskai, M.A., Afonin, K.A., 2022. Expanding structural space for immunomodulatory nucleic acid nanoparticles (NANPs) via spatial arrangement of their therapeutic moieties. Adv. Funct. Mater. 32, 2205581. https://doi.org/10.1002/adfm.202205581.
Christodoulou, I., Bourguignon, T., Li, X., Patriarche, G., Serre, C., Marlière, C., Gref, R., 2021. Degradation mechanism of porous metal-organic frameworks by in situ atomic force microscopy. Nanomaterials 11, 722. https://doi.org/10.3390/nano11030722.
Cutrone, G., Li, X., Casas-Solvas, J.M., Menendez-Miranda, M., Qiu, J., Benkovics, G., Constantin, D., Malanga, M., Moreira-Alvarez, B., Costa-Fernandez, J.M., García-Fuentes, L., Gref, R., Vargas-Berenguel, A., 2019a. Design of engineered cyclodextrin derivatives for spontaneous coating of highly porous metal-organic framework nanoparticles in aqueous media. Nanomaterials. 1103, 1–26. https://doi.org/10.3390/nano9081103.
Cutrone, G., Qiu, J., Menendez-Miranda, M., Casas-Solvas, J.M., Aykaç, A., Li, X., Foulkes, D., Moreira-Alvarez, B., Encinar, J.R., Ladavière, C., Desmaële, D., Vargas-Berenguel, A., Gref, R., 2019b. Comb-like dextran copolymers: a versatile strategy to coat highly porous MOF nanoparticles with a PEG shell. Carbohydr. Polym. 223, 115085 https://doi.org/10.1016/j.carbpol.2019.115085.
Ding, M., Liu, W., Gref, R., 2022. Nanoscale MOFs: from synthesis to drug delivery and theranostics applications. Adv. Drug Deliv. Rev. 190, 114496 https://doi.org/10.1016/j.addr.2022.114496.
Ettlinger, R., Lächelt, U., Gref, R., Horcajada, P., Lammers, T., Serre, C., Couvreur, P., Morris, R.E., Wuttke, S., 2022. Toxicity of metal-organic framework nanoparticles: from essential analyses to potential applications. Chem. Soc. Rev. 51, 464–484. https://doi.org/10.1039/D1CS00918D.
Férey, G., Mellot-Draznieks, C., Serre, C., Millange, F., Dutour, J., Surblé, S., Margiolaki, I., 2005. A chromium terephthalate-based solid with unusually large pore volumes and surface area. Science 309, 2040–2042. https://doi.org/10.1126/science.1116275.
Gimenez-Marques, M., Bellido, E., Berthelot, T., Simon-Yarza, T., Hidalgo, T., Simón-Vázquez, R., González-Fernández, A., Avila, J., Asensio, M.C., Gref, R., Couvreur, P.,

Christian Serre, C., Horcajada, P., 2018. Metal-organic framework surface functionalization: GraftFast surface engineering to improve MOF nanoparticles furtiveness. Small 40, 1870182. https://doi.org/10.1002/smll.201870182.

Grossen, P., Witzigmann, D., Sieber, S., Huwyler, J., 2017. PEF-PCL-based nanomedicines: a biodegradable drug delivery system and its application. J. Control. Release 260, 46–60. https://doi.org/10.1016/j.jconrel.2017.05.028.

Halman, J.R., Kim, K.T., Gwak, S.J., Pace, R., Johnson, M.B., Chandler, M.R., Rackley, L., Viard, M., Marriott, I., Lee, J.S., Afonin, K.A., 2020. A cationic amphiphilic co-polymer as a carrier of nucleic acid nanoparticles (Nanps) for controlled gene silencing, immunostimulation, and biodistribution. Nanomedicine. 23, 102094 https://doi.org/10.1016/j.nano.2019.102094.

He, C., Lu, K., Liu, D., Lin, W., 2014. Nanoscale metal–organic frameworks for the co-delivery of cisplatin and pooled siRNAs to enhance therapeutic efficacy in drug-resistant ovarian cancer cells. J. Am. Chem. Soc. 136, 5181–5184. https://doi.org/10.1021/ja4098862.

He, S., Wu, L., Li, X., Sun, H., Xiong, T., Liu, J., Huang, C., Xu, H., Su, H., Chen, W., Gref, R., Zhang, J., 2021. Metal-organic frameworks for advanced drug delivery. Acta Pharm. Sin. B 8, 2362–2395. https://doi.org/10.1016/j.apsb.2021.03.019.

Horcajada, P., Chalati, T., Serre, C., Gillet, B., Sebrie, C., Baati, T., Eubank, J.F., Heurtaux, D., Clayette, P., Kreuz, C., Chang, J., Hwang, Y.K., Marsaud, V., Bories, P., Cynober, L., Couvreur, P., Gref, R., 2009. Porous metal–organic-framework nanoscale carriers as a potential platform for drug delivery and imaging. Nat. Mater. 9, 172–178. https://doi.org/10.1038/NMAT2608.

Jackson, L.A., Anderson, E.J., Rouphael, N.G., Roberts, P.C., Makhene, M., Coler, R.N., McCullough, M.P., Chappell, J.D., Denison, M.R., Stevens, L.J., Pruijssers, A.J., McDermott, A., Flach, B., Doria-Rose, N.A., Corbett, K.S., Morabito, K.M., O'Dell, S., Schmidt, S.D., Swanson, P.A., Padilla, M., Mascola, J.R., Neuzil, K.M., Bennett, H., Sun, W., Peters, E., Makowski, M., Albert, J., Cross, K., Buchanan, W., Pikaart-Tautges, R., Ledgerwood, J.E., Graham, B.S., Beigel, J.H., 2020. An mRNA vaccine against SARS-CoV-2 -preliminary report. N. Engl. J. Med. 383, 1920–1931. https://doi.org/10.1056/NEJMoa2022483.

Johnson, M.B., Chandler, M., Afonin, K.A., 2021. Nucleic acid nanoparticles (NANPs) as molecular tools to direct desirable and avoid undesirable immunological effects. Adv. Drug Deliv. Rev. 173, 427–438. https://doi.org/10.1016/j.addr.2021.04.011.

Juneja, R., Lyles, Z., Vadarevu, H., Afonin, K.A., Vivero-Escoto, J.L., 2019. Multimodal polysilsesquioxane nanoparticles for combinatorial therapy and gene delivery in triple-negative breast cancer. ACS Appl. Mater. Interfaces 11, 12308–12320. https://doi.org/10.1021/acsami.9b00704.

Juneja, R., Vadarevu, H., Halman, J., Tarannum, M., Rackley, L., Dobbs, J., Marquez, J., Chandler, M., Afonin, K., Vivero-Escoto, J.L., 2020. Combination of nucleic acid and mesoporous silica nanoparticles: optimization and therapeutic performance in vitro. ACS Appl. Mater. Interfaces 12, 38873–38886. https://doi.org/10.1021/acsami.0c07106.

Ke, W., Afonin, K.A., 2021. Exosomes as natural delivery carriers for programmable therapeutic nucleic acid nanoparticles (NANPs). Adv. Drug Deliv. Rev. 176, 113835 https://doi.org/10.1016/j.addr.2021.113835.

Kim, T., Viard, M., Afonin, K.A., Gupta, K., Popov, M., Salotti, J., Johnson, P.F., Linder, C., Heldman, E., Shapiro, B.A., 2020. Characterization of cationic bolaamphiphile vesicles for siRNA delivery into tumors and brain. Mol. Ther. Nucl. Acids 20, 359–372. https://doi.org/10.1016/j.omtn.2020.02.011.

Kulkarni, J.A., Witzigmann, D., Thomson, S.B., Chen, S., Leavitt, B.R., Cullis, P.R., Van der Meel, R., 2021. The current landscape of nucleic acid therapeutics. Nat. Nanotechnol. 16, 630–643. https://doi.org/10.1038/s41565-021-00898-0.

Li, X., Lachmanski, L., Safi, S., Sene, S., Serre, C., Grenèche, J.M., Zhang, J., Gref, R., 2017. New insights into the degradation mechanism of metal-organic frameworks drug carriers. Sci. Rep. 7, 13142. https://doi.org/10.1038/s41598-017-13323-1.

Li, X., Porcel, E., Menendez-Miranda, M., Qiu, J., Yang, X., Serre, C., Pastor, A., Desmaele, D., Lacombe, S., Gref, R., 2020a. Highly porous hybrid metal-organic nanoparticles loaded with gemcitabine monophosphate: a multimodal approach to improve chemo- and radiotherapy. ChemMedChem 15, 274–283. https://doi.org/10.1002/cmdc.201900596.

Li, X., Porcino, M., Martineau-Corcos, C., Guo, T., Xiong, T., Zhu, W., Patriarche, G., Péchoux, C., Perronne, B., Hassan, A., Kümmerle, R., Michelet, A., Zehnacker-Rentien, A., Zhang, J., Gref, R., 2020b. Efficient incorporation and protection of lansoprazole in cyclodextrin metal-organic frameworks. Int. J. Pharmaceut. 585, 119442 https://doi.org/10.1016/j.ijpharm.2020.119442.

Li, X., Salzano, G., Qiu, J., Menard, M., Berg, K., Theodossiou, T., Ladavière, C., Gref, R., 2020c. Drug-loaded lipid-coated hybrid organic-inorganic "stealth" nanoparticles for cancer therapy. Front. Bioeng. Biotechnol. 1027, 1–12. https://doi.org/10.3389/fbioe.2020.01027.

Lin, H., Hsu, K., Lai, C., Wu, T., Chen, H., Lai, C., 2020. Mannoside-modified branched gold nanoparticles for photothermal therapy to MDA-MB-231 cells. Molecules 25, 1853. https://doi.org/10.3390/molecules25081853.

Mokhtarian, F., Rastegari, B., Zeinali, S., Tohidi, M., Karbalaei-Heidari, H.R., 2022. Theranostic effect of folic acid functionalized MIL-100(Fe) for delivery of prodigiosin and simultaneous tracking-combating breast cancer. J. Nanomater. 2022, 1108865 https://doi.org/10.1155/2022/1108865.

Nguyen, T., Francis, M.B., 2003. Practical synthetic route to functionalized rhodamine dyes. Org. Lett. 5, 3245–3248. https://doi.org/10.1021/ol035135z.

Ni, Q., Lin, J., Zhang, N., Li, S., Xue, Y., Wang, Z., Liu, Q., Liu, K., Zhang, H., Zhao, Y., Chen, C., Liu, Y., 2022. Combinational application of metal-organic frameworks-based nanozyme and nucleic acid delivery in cancer therapy. WIREs Nanomed. Nanobiotechnol. 14, e1773 https://doi.org/10.1002/wnan.1773.

Nordmeier, S., Ke, W., Afonin, K.A., Portnoy, V., 2020. Exosome mediated delivery of functional nucleic acid nanoparticles (NANPs). Nanomed. Nanotechnol. Biol. Med. 30, 102285 https://doi.org/10.1016/j.nano.2020.102285.

Pancani, E., Mathurin, J., Bilent, S., Bernet-Camard, M.F., Dazzi, A., Deniset-Besseau, A., Gref, R., 2018. High-resolution label-free detection of biocompatible polymeric nanoparticles in cells. Part. Part. Syst. Charact. 35, 1700457. https://doi.org/10.1002/ppsc.201700457.

Panigaj, M., Dobrovolskaia, M.A., Afonin, K.A., 2021. An immunotherapy odyssey and the rise of nucleic acid nanotechnology. Nanomedicine. 16, 1635–1640. https://doi.org/10.2217/nnm-2021-0097.

Peng, S., Bie, B., Sun, Y., Liu, M., Cong, H., Zhou, W., Xia, Y., Tang, H., Deng, H., Zhou, X., 2018. Metal-organic frameworks for precise inclusion of single-stranded DNA and transfection in immune cells. Nat. Commun. 9, 1293. https://doi.org/10.1038/s41467-018-03650-w.

Qiu, J., Li, X., Gref, R., Vargas-Berenguel, A., 2020a. Carbohydrates in metal organic frameworks: Supramolecular assembly and surface modification for biomedical applications. In: Mozafari, M. (Ed.), Metal Organic Frameworks for Biomedical Applications, pp. 445–465. https://doi.org/10.1016/B978-0-12-816984-1.00022-6.

Qiu, J., Li, X., Steenkeste, K., Barroca-Aubry, N., Aymes-Chodur, C., Roger, P., Casas-Solvas, J.M., Vargas-Berenguel, A., Rihouey, C., Picton, L., Gref, R., 2020b. Self-assembled multifunctional core-shell highly porous metal-organic framework nanoparticles. Int. J. Pharmaceut. 581, 119281 https://doi.org/10.1016/j.ijpharm.2020.119281.

Qiu, J., Li, X., Rezaei, M., Patriarche, G., Casas-Solvas, J.M., Moreira-Alvarez, B., Fernandez, J.M.C., Encinar, R., Savina, F., Picton, L., Vargas-Berenguel, A., Gref, R., 2021. Porous nanoparticles with engineered shells release their drug cargo in cancer cells. Int. J. Pharmaceut. 610, 121230 https://doi.org/10.1016/j.ijpharm.2021.121230.

Rackley, L., Stewart, J.M., Salotti, J., Krokhotin, A., Shah, A., Halman, J.R., Juneja, R., Smollett, J., Lee, L., Roark, K., Viard, M., Tarannum, M., Vivero-Escoto, J., Johnson, P.F., Dobrovolskaia, M.A., Dokholyan, N.V., Franco, E., Afonin, K.A., 2018. RNA fibers as optimized nanoscaffolds for siRNA coordination and reduced immunological recognition. Adv. Funct. Mater. 28, 1805959. https://doi.org/10.1002/adfm.201805959.

Rodriguez-Ruiz, V., Maksimenko, A., Anand, R., Monti, S., Agostoni, V., Couvreur, P., Lampropoulou, M., Yannakopoulou, K., Gref, R., 2015. Efficient "green" encapsulation of a highly hydrophilic anticancer drug in metal-organic framework nanoparticles. J. Drug Target. 23, 759–767. https://doi.org/10.3109/1061186X.2015.1073294.

Rose, S.D., Kim, D., Amarzguioui, M., Heidel, J.D., Collingwood, M.A., Davis, M.E., Rossi, J.J., Behlke, M.A., 2005. Functional polarity is introduced by dicer processing of short substrate RNAs. Nucleic Acids Res. 33, 4140–4156. https://doi.org/10.1093/nar/gki732.

Simon-Yarza, T., Baati, T., Neffati, F., Njim, L., Couvreur, P., Serre, C., Gref, R., Najjar, M.F., Zakhama, A., Horcajada, P., 2016. In vivo behavior of MIL-100 nanoparticles at early times after intravenous administration. Int. J. Pharmaceut. 511, 1042–1047. https://doi.org/10.1016/j.ijpharm.2016.08.010.

Simon-Yarza, T., Giménez-Marqués, S., Mrimi, R., Mielcarek, A., Gref, R., Horcajada, P., Serre, C., Couvreur, P., 2017. A smart metal–organic framework nanomaterial for lung targeting. Angew. Chem. 56 (49), 15565–15569. https://doi.org/10.1002/anie.201707346.

Sun, Y., Zheng, L., Yang, Y., Qian, X., Fu, T., Li, X., 2020. Metal–organic framework nanocarriers for drug delivery in biomedical applications. Nano-Micro Lett. 12, 103. https://doi.org/10.1007/s40820-020-00423-3.

Sun, Q., Hou, X., Yang, J., Zhang, M., Yang, Y., Liu, Y., Shen, W., Yin, D., 2021. Heparin-coated photosensitive metal–organic frameworks as drug delivery nanoplatforms of autophagy inhibitors for sensitized photodynamic therapy against breast cancer. ACS Appl. Mater. Interfaces 13, 55577–55590. https://doi.org/10.1021/acsami.1c18055.

Teplensky, M.H., Fantham, M., Poudel, C., Hockings, C., Lu, M., Guna, A., Aragones-Anglada, M., Moghadam, P.Z., Li, P., Farha, O.K., de Quirós Fernández, S.B., Richards, F.M., Jodrell, D.I., Kaminski Schierle, G., Kaminski, C.F., Fairen-Jimenez, D., 2019. A highly porous metal-organic framework system to deliver payloads for gene knockdown. Chem. 5, 2926–2941. https://doi.org/10.1016/j.chempr.2019.08.015.

Wang, L., Zheng, M., Xie, Z., 2018. Nanoscale metal-organic frameworks for drug delivery: a conventional platform with new promise. J. Mater. Chem. B 6, 707–717. https://doi.org/10.1039/C7TB02970E.

Wang, X., Ruifang, L., Yongxiz, Z., Wang, Z., Zhang, H., Cui, L., Duan., Guo, Y., 2020. Active targeting co-delivery of therapeutic Sur siRNA and an antineoplastic drug via epidermal growth factor receptor-mediated magnetic nanoparticles for synergistic programmed cell death in glioblastoma stem cells. Mater. Chem. Front. 4, 574. https://doi.org/10.1039/c9qm00666d.

Wang, J., Yu, K., Ji, X., Bai, H., Zhang, W., Hu, X., Tang, G., 2021. Structural insights into the host-guest complexation between β-cyclodextrin and bio-conjugatable adamantane derivatives. Molecules. 26, 2412. https://doi.org/10.3390/molecules26092412.

Xin, X., Kumar, V., Lin, F., Kumar, V., Bhattarai, R., Bhatt, V.R., Tan, C., Mahato, R.I., 2020. Redox-responsive nanoplatform for codelivery of miR-519c and gemcitabine for pancreatic cancer therapy. Sci. Adv. 6, eabd6764. https://doi.org/10.1126/sciadv.abd6764.

Zhang, Y., Schwerbrock, N.M., Rogers, A.B., Kim, W.Y., Huang, L., 2013. Codelivery of VEGF siRNA and gemcitabine monophospate in a single nanoparticle formulation for effective treatment of NSCLC. Mol. Ther. 21, 1559–1569. https://doi.org/10.1038/mt.2013.120.